A Modeling Study of Diurnal Rainfall Variations during the 21-Day Period of TOGA COARE

GAO Shouting[*1] (高守亭), CUI Xiaopeng[1] (崔晓鹏), and Xiaofan LI[2]

[1]*Laboratory of Cloud-Precipitation Physics and Severe Storms (LACS),*

Institute of Atmospheric Physics, Chinese Academy of Sciences, Beijing 100029

[2]*Joint Center for Satellite Data Assimilation and NOAA/NESDIS/Center for*

Satellite Applications and Research, Camp Springs, Maryland, USA

ABSTRACT

The surface rainfall processes and diurnal variations associated with tropical oceanic convection are examined by analyzing a surface rainfall equation and thermal budget based on hourly zonal-mean data from a series of two-dimensional cloud-resolving simulations. The model is integrated for 21 days with imposed large-scale vertical velocity, zonal wind, and horizontal advection obtained from the Tropical Ocean Global Atmosphere Coupled Ocean-Atmosphere Response Experiment (TOGA COARE) in the control experiment. Diurnal analysis shows that the infrared radiative cooling after sunset, as well as the advective cooling associated with imposed large-scale ascending motion, destabilize the atmosphere and release convective available potential energy to energize nocturnal convective development. Substantial local atmospheric drying is associated with the nocturnal rainfall peak in early morning, which is a result of the large condensation and deposition rates in the vapor budget. Sensitivity experiments show that diurnal variations of radiation and large-scale forcing can produce a nocturnal rainfall peak through infrared and advective cooling, respectively.

1. Introduction

The diurnal variation of tropical oceanic convection is one of the important signals in tropical variability and plays a crucial role in regulating tropical hydrological and energy cycles. The dominant diurnal signal exhibits a nocturnal peak in rainfall that occurs in the early morning over the tropical open ocean and land. Kraus (1963) analyzed observational rainfall data and showed nocturnal rainfall peaks, suggesting that solar heating suppresses convection during the daytime, whereas infrared cooling enhances convection during the nighttime. Gray and Jacobson (1977) found that heavy rainfall is much larger in the morning than in the late afternoon and evening, and argued that the radiational differences between cloudy regions and clear-sky regions play an important role in enhancing a secondary circulation and thus the nocturnal rainfall. Randall et al. (1991) carried out sensitivity experiments using a general circulation model and showed that in the absence of cloud radiative effects, the phase of simulated diurnal rainfall cycle is not changed but the amplitude is much weakened. Xu and Randall (1995) conducted sensitivity experiments with a cloud-resolving model and revealed that the diurnal variation is not sensitive to interactive radiation and that Gray and Jacobson's mechanism plays a secondary role in diurnal processes.

Tao et al. (1996) carried out a series of cloud-resolving simulations to study cloud-radiation interaction mechanisms and emphasized that the nocturnal precipitation is enhanced by infrared cooling through

*Corresponding author: GAO Shouting, gst@lasg.iap.ac.cn

increasing relative humidity. The surface rainfall is not sensitive to cloud-top cooling, cloud-base warming, or the differential cooling between clear-sky and cloudy regions. Sui et al. (1997) conducted an observational analysis during the Tropical Ocean Global Atmosphere Coupled Ocean-Atmosphere Response Experiment (TOGA COARE) to study the diurnal rainfall processes and suggested that the nocturnal rainfall peak is a result of the destabilization by radiative cooling during the nighttime, with the falling temperature increasing the available precipitable water for precipitation. Liu and Moncrieff (1998) found from their cloud-resolving simulations that the simulated diurnal rainfall variation is primarily caused by direct cloud-radiation interaction, and that Gray and Jacobson's mechanism is a secondary factor. Sui et al. (1998) conducted cloud-resolving simulations to test their nocturnal rainfall mechanism and their numerical experiments support Sui et al. (1997) suggestions. Petch and Gray (2001) conducted sensitivity studies using a cloud-resolving model and showed that the simulated diurnal rainfall cycle of the tropical west Pacific is determined by large-scale forcing but is not enhanced by radiation. Dai (2001) analyzed 3-hourly precipitation data from Global Telecommunication System (GTS) stations and from the Comprehensive Ocean-Atmosphere Data Set (COADS) and emphasized the importance of land-ocean contrast in the formation of a nocturnal precipitation peak over the coastal areas. Thus, the diurnal variations of radiation and large-scale forcing account for the nocturnal rainfall peak over the tropical ocean.

Although numerical experiments highlight important processes that qualitatively determine the diurnal rainfall cycle, important diurnal rainfall processes have not been studied quantitatively. Gao et al. (2005) derived a diagnostic surface rainfall equation to study precipitation processes. The surface rain rate is simply formulated with the sum of water vapor and cloud sources/sinks. They analyzed the surface rain rate using hourly zonal-mean simulation data from a two-dimensional (2D) cloud-resolving model and found that although the water vapor sink (water vapor convergence, surface evaporation, and local atmospheric drying) largely accounts for the variation of the surface rain rate, cloud sources/sinks could significantly modify the surface rain rate. Their results show that this surface rainfall equation can be used to quantitatively identify the dominant physical processes in precipitation.

In this study, a series of experiments are conducted using a 2D cloud-resolving model to examine physical processes such as radiation and large-scale forcing that are responsible for the nocturnal rainfall peak. In the control experiment, large-scale forcing data derived from TOGA COARE are imposed. Since zonally averaged large-scale forcing (vertical velocity, zonal wind, and horizontal advection) and SST may include diurnal signals and the model includes an interactive radiation calculation, a series of sensitivity experiments are carried out. With the analysis of the cloud, water vapor, and heat budget, the sensitivity experiments are compared with the control experiment to quantitatively evaluate the effects of diurnal variations of vertical velocity, SST, and radiation on the formation of the nocturnal rainfall peak. In the next section, the cloud model, forcings, and experiments are described and the surface rainfall equation and thermal budget are presented. The control case is discussed and compared with the observations in terms of thermodynamics and surface rainfall, and the analysis of physical processes associated with the diurnal rainfall variation is carried out in section 3. The dominant physical processes that are responsible for the nocturnal peak of surface rainfall are further identified with additional sensitivity experiments in section 4. The summary is given in section 5.

2. Model and experimental design

The Goddard Cumulus Ensemble Model (Soong and Ogura, 1980; Soong and Tao, 1980; Tao and Simpson, 1993) used here is the 2D version (Sui et al., 1994, 1998) modified by Li et al. (1999). The model has five prognostic equations for the mixing ratios of cloud hydrometeors (cloud water, raindrops, cloud ice, snow, and graupel). The model also includes the cloud microphysical parameterization schemes from Rutledge and Hobbs (1983, 1984), Lin et al. (1983), Tao et al. (1989), Krueger et al. (1995), as well as interactive radiation calculations performing solar (Chou et al., 1998) and thermal infrared (Chou et al., 1991; Chou and Suarez, 1994) radiation parameterization schemes every 3 minutes. The model uses cyclic lateral boundaries. The vertical velocity, vertical gradients of potential temperature, specific humidity, and mixing ratios of cloud hydrometeors in the model are set to zero at both the upper and lower boundaries (Soong and Ogura, 1980). The surface momentum, heat, and evaporation fluxes are calculated from bulk formulations using predicted wind, temperature, and specific humidity (Soong and Ogura, 1980). The basic model parameters include a horizontal domain of 512 grid points, a horizontal grid resolution of 1.5 km, a top model level of 42 hPa, and a time step of 12 s. The vertical grid resolution ranges from about 200 m near the surface to about 1 km near 100 hPa. The 2D cloud-resolving model simulation has been validated
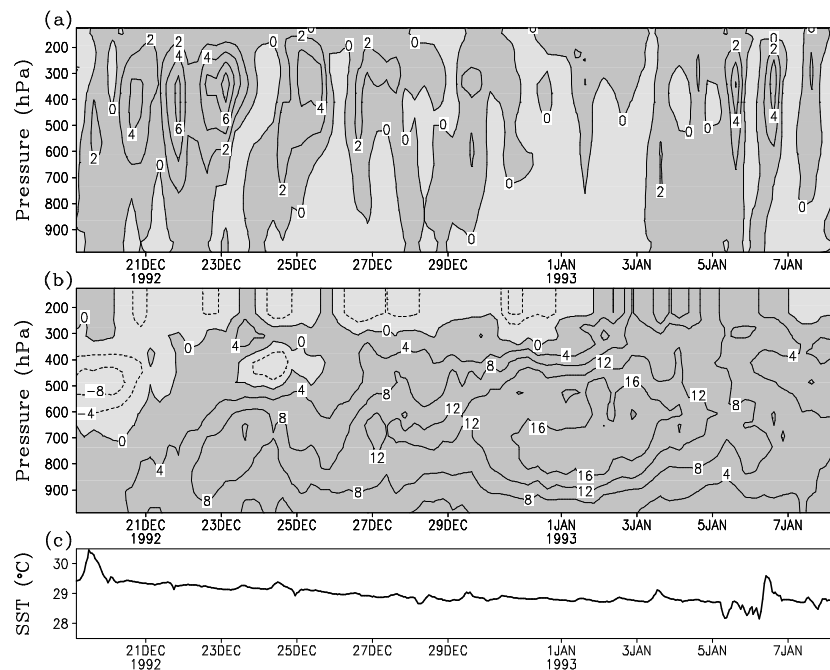
Fig. 1. Temporal and vertical distributions of (a) vertical velocity (cm s^{-1}), (b) zonal wind (m s^{-1}), and time series of (c) sea surface temperature ($^{\circ}$C) observed and derived from TOGA COARE for the 21-day period.

with observations in terms of atmospheric thermodynamic profiles, surface fluxes, and surface rain rate in the tropics during TOGA COARE (Li et al., 1999). This model and other cloud resolving models have been applied to tropical thermodynamic, cloud, and surface rainfall studies during the Global Atmospheric Research Program Atlantic Tropical Experiment (GATE) (e.g., Xu and Randall, 1996; Grabowski et al., 1996) and TOGA COARE (e.g., Wu et al., 1998; Li et al., 2002a,b,c; Gao et al., 2004, 2005, 2006a,b).

In the control case, the zonally-uniform vertical velocity, zonal wind, and thermal and moisture advection (Fig. 1) observed and derived from 6-hourly TOGA COARE observations within the Intensive Flux Array (IFA) region are linearly interpolated and imposed in the model at every time step during the integrations. This observational data is provided by the research group of Prof. M. Zhang at The State University of New York at Stony Brook. They applied a constrained, variational method to column-integrated budgets of mass, heat, moisture, and momentum in their data analysis (Zhang and Lin, 1997). Hourly SST at the Improved Meteorological (IMET) surface mooring buoy (1.75°S, 156°E) from Weller et al. (1996) is also imposed in the model. The model was integrated from 0400 LST 18 December 1992 to 1000 LST 9 January 1993 (a total of 21.25 days or 486 hours). The 21-day study period covers the life span of a westerly wind burst with strong ascending motion during the onset

and decay phases, with weak descending motions during the peak phase. A portion of study period (20–26 December 1992) has been intensively analyzed and discussed by the Global Energy and Water Cycle Experiment (GEWEX) Cloud System Study (GCSS) Working Group 4 (Moncrieff et al., 1997; Krueger, 1997). A diurnal composite of vertical profiles of imposed large-scale vertical velocity (Fig. 2) shows a strong diurnal variation with maximum ascending motion of 3 cm s^{-1} at 1600 LST around 340 hPa, and minimum ascending motion of less than 1 cm s^{-1} at 0400 LST. Note that the maximum ascending motion is not in phase with nocturnal rainfall peak.

Since the diurnal rainfall variations may be caused by various factors including large-scale forcing, radiative process, and SST, four additional sensitivity experiments were designed (Table 1). In the radiation-only case, the model uses diurnally varying interactive radiation calculations and imposed time-mean large-scale vertical velocity, zonal wind, horizontal advection, and SST. In the large-scale forcing-only case, a time-invariant solar zenith angle with a daily average cosine value is used in interactive radiation calculations, and time-mean SST and diurnally varying large-scale vertical velocity, zonal wind, and horizontal advection are imposed in the model. In the SST-only case, a time-invariant solar zenith angle is used in interactive radiation calculations, and time-mean large-scale vertical velocity, zonal wind, and horizontal ad-

Table 1. A summary of experiments.

	Radiation	Large-scale vertical velocity	Large-scale zonal wind	SST
Control case	Diurnally varying	Varied	Varied	Varied
Radiation-only case	Diurnally varying	Time-mean	Time-mean	Time-mean
Large-scale forcing-only case	A constant with a daily average cosine value	Varied	Varied	Time-mean
SST-only case	A constant with a daily average cosine value	Time-mean	Time-mean	Varied
Radiation-only case with zero large-scale vertical velocity	Diurnally varying	Zero	A constant of 4 m s^{-1}	Time-mean

vection and diurnally varying SST are imposed in the model. Thus, the radiation-only, large-scale forcing-only, and SST-only cases are each compared to the control case to examine the effects of diurnal variations of radiation, vertical velocity, and SST on the formation of the nocturnal rainfall peak. Since vertical velocity is a major forcing imposed in the model and may vary when it is derived from different regions and periods or averaged over different sizes of areas, another radiation-only case is tested with imposed zero vertical velocity, horizontal advection, and mean zonal wind. The mean zonal wind is 4 m s^{-1} since the minimum wind speed in the calculations of surface heat fluxes is 4 m s^{-1}.

Following Gao et al. (2005), zonal-mean surface rain rate (P_s) can be symbolically expressed as

$$P_s = Q_{WVT} + Q_{WVF} + Q_{WVE} + Q_{CM}. \quad (1)$$

Here, $Q_{WVT} = -\dfrac{\partial [q_v]}{\partial t}$ is local water vapor tendency. $Q_{WVF} = -[\overline{u}^o \dfrac{\partial \overline{q}_v^o}{\partial x}] - [\overline{w}^o \dfrac{\partial \overline{q}_v}{\partial z}]$ is water vapor advection, and a major forcing comes from the vertical advective moistening/drying term, since the imposed horizontal vapor advection is smaller than vertical advection. $Q_{WVE} = E_s$ is the surface evaporation rate. $Q_{CM} =$

Fig. 2. Diurnal composite of vertical profile of vertical velocity (cm s^{-1}) imposed in the model simulation.

$-\dfrac{\partial [q_5]}{\partial t}$ is the local hydrometeor change in the cloud microphysical budget, where the condition that $-[u\dfrac{\partial q_5}{\partial x}] - [w\dfrac{\partial q_5}{\partial z}] = 0$ is used as a result of cyclic boundary conditions. In Eq. (1), q_v is atmospheric specific humidity, u and w are zonal and vertical wind components, respectively, $q_5 = q_c + q_r + q_i + q_s + q_g$, and q_c, q_r, q_i, q_s, q_g are the mixing ratios of cloud water, raindrops, cloud ice, snow, and graupel, respectively. Overbars and superscripts (^{o}) denote a zonal-mean and an imposed observed value, respectively. A zonal-mean mass integration of a variable F is defined by

$$[F] = \frac{1}{512} \sum_{i=1}^{512} \int_0^{z_t} F_i \overline{\rho} dz, \quad (1a)$$
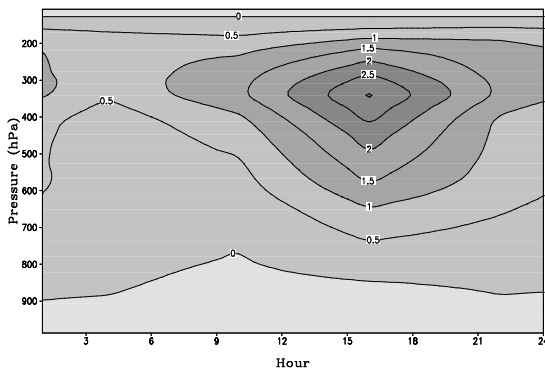
where z_t is the model top.

The thermal budget can be expressed as

$$S_H + S_{HF} + S_{HS} + S_{LH} + S_{RAD} = 0. \quad (2)$$

Here, $S_{HT} = -\dfrac{\partial <T>}{\partial t}$ is local heat tendency. $S_{HF} = -<\overline{u}^o \dfrac{\overline{T}^o}{\partial x}> - <\pi \overline{w}^o \dfrac{\partial \overline{\theta}}{\partial z}>$ is thermal convergence, including a major forcing from vertical advective cooling/warming, since imposed horizontal thermal advection is much smaller than vertical advection. S_{HS} is surface sensible heat flux. $S_{LH} = \dfrac{1}{c_p} <Q_{cn}>$ is the net latent heat release through phase changes among different cloud species. $S_{RAD} = \dfrac{1}{c_p} <Q_R>$ is the radiative heating rate due to the convergence of net flux of solar and infrared radiative fluxes. In Eq. (2), T and θ are air temperature and potential temperature, respectively, and is the specific heat of dry air at constant pressure. A zonal and mass-weighted mean of a variable $<F>$ is defined by

$$<F> = \frac{1}{512} \sum_{i=1}^{512} \int_0^{z_t} F_i \overline{\rho} dz \int_0^{z_t} \overline{\rho} dz. \quad (2a)$$

The variance of zonal-mean surface rain rate can

be expressed by

$$\mathrm{Var}(P_s) = \mathrm{Var}(Q_\mathrm{WVT}) + \mathrm{Var}(Q_\mathrm{WVF}) + \mathrm{Var}(Q_\mathrm{WVE}) +$$
$$\mathrm{Var}(Q_\mathrm{CM}) + 2\mathrm{CoVar}(Q_\mathrm{WVT}, Q_\mathrm{WVF}) +$$
$$2\mathrm{CoVar}(Q_\mathrm{WVT}, Q_\mathrm{WVE}) +$$
$$2\mathrm{CoVar}(Q_\mathrm{WVT}, Q_\mathrm{CM}) +$$
$$2\mathrm{CoVar}(Q_\mathrm{WVF}, Q_\mathrm{WVE}) +$$
$$2\mathrm{CoVar}(Q_\mathrm{WVF}, Q_\mathrm{CM}) +$$
$$2\mathrm{CoVar}(Q_\mathrm{WVE}, Q_\mathrm{CM}), \quad (3)$$

where

$$\mathrm{Var}(A) = \frac{1}{486} \sum_{i=1}^{486} (A_i - A)^2, \quad (3a)$$

$$\mathrm{CoVar}(A, B) = \frac{1}{486} \sum_{i=1}^{486} (A_i - A)(B_i - B), \quad (3b)$$

$$A = \frac{1}{486} \sum_{i=1}^{486} A_i. \quad (3c)$$

3. Analysis of diurnal variations with control simulation

The control simulation is compared with the observations in terms of temperature, specific humidity, and surface rain rate. The root-mean-squared (RMS) differences in temperature and specific humidity between the observations and control experiment over vertical and horizontal model domains are 1.66°C and 0.5 g kg^{-1}, respectively, which are slightly larger than those in the 7-day comparison during TOGA COARE (Li et al., 1999). The observed surface rain rate is derived by averaging over a 150×150 km^2 area using radar reflectivity data taken from the Massachusetts Institute of Technology's Doppler radar and the TOGA radar located within the Intensive Flux Array (IFA) region (Short et al., 1997). The RMS difference in surface rain rate between the observations and control experiment is 0.43 mm h^{-1}, which is similar to the standard deviation of simulated surface rain rate (0.43 mm h^{-1}) and is larger than the standard deviation of observed surface rain rate (0.37 mm h^{-1}). The large RMS difference may be caused by the inconsistency between the surface rain rate and imposed vertical velocity. For example, the surface rain rate on 20 December 1992 is larger than that on 21–22 December 1992 (Fig. 3a), whereas the upward motion on 20 December 1992 is weaker than that on 21–22 December 1992 (Fig. 1a). The diurnal composites of observed and simulated surface rain rates show that the largest periods of rainfall occur during early morning, late afternoon, and evening (Fig. 5). The differences in the diurnal composites of surface rain rates between the observations

and control experiment are that the simulated surface rain rate is larger than the observed surface rain rate and that the simulated surface rain rate reaches its minimum 3 hours earlier than does the observed surface rain rate. The comparison reveals that the 21-day model simulation agrees reasonably well with the observations.

Figure 3 shows the time series of P_s, Q_WVT, Q_WVF, Q_WVE and Q_CM. The time-means of P_s, Q_WVT, Q_WVF, Q_WVE and Q_CM are 0.37, 0.03, 0.12, 0.2, and 0.02 mm h^{-1}, respectively. Q_WVT, Q_WVF, Q_WVE and Q_CM contribute 8.1%, 32.4%, 54.1%, and 5.4% to P_s, respectively. The amplitudes of variations of Q_WVT and Q_CM are much larger than for Q_WVE. Q_WVE is always positive, whereas Q_WVT and Q_CM change signs frequently, which leads to cancellations in time-mean calculations. Thus, Q_WVE is the largest term contributing to the time-mean of P_s. The surface evaporation rate and vapor convergence associated with the imposed vertical velocity mainly contribute to the tem-
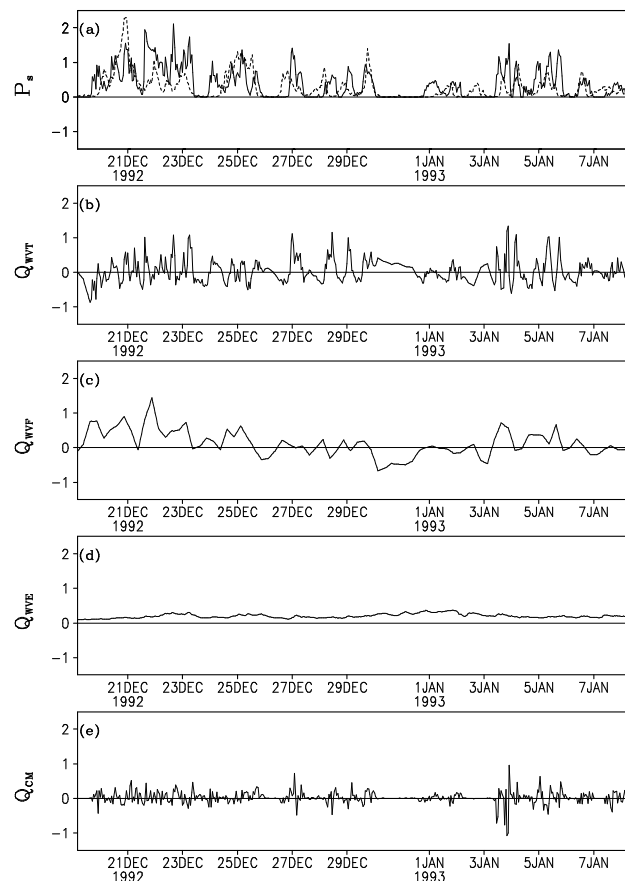

Fig. 3. Time series of (a) P_s, (b) Q_WVT, (c) Q_WVF, (d) Q_WVE, and (e) Q_CM simulated in the control case during the 21-day integration. Units are mm h^{-1}. Dashed line in (a) denotes observed P_s.
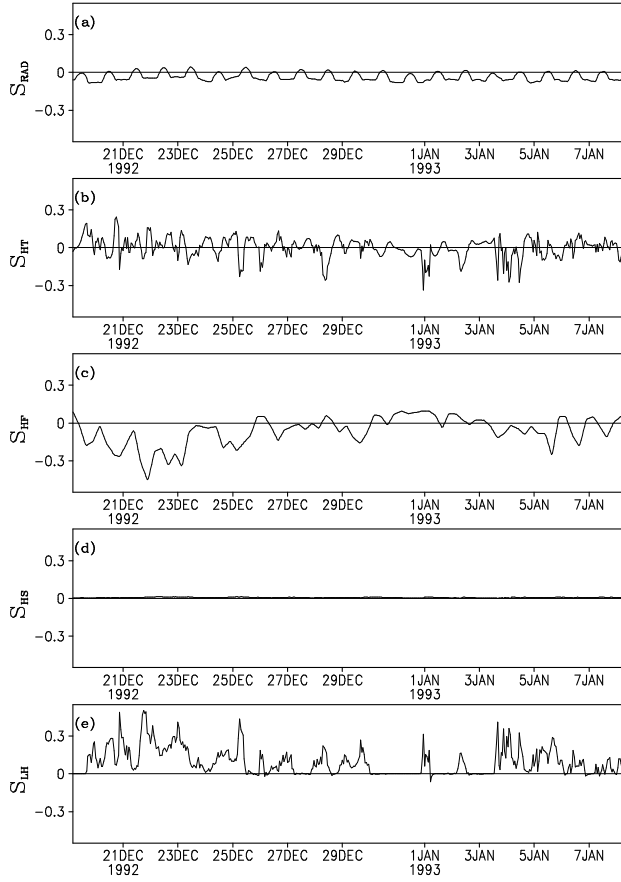
Fig. 4. Time series of (a) S_{RAD}, (b) S_{HT}, (c) S_{HF}, (d) S_{HS}, and (e) S_{LH} in the control case during the 21-day integration. Units are $^{\circ}\mathrm{C}\,\mathrm{h}^{-1}$.

poral and zonal mean surface rain rate. Cui and Li (2006) analyzed the data from 2D cloud-resolving model simulations with an imposed zero vertical velocity and found that the temporal and zonal-mean surface evaporation mainly comes from rainfall-free regions. Surface evaporation pumps water vapor into rainfall-free regions and the divergence transports the vapor from rainfall-free regions to heavier rainfall regions.

The variance of surface rain rate ($0.18\,\mathrm{mm}^2\,\mathrm{h}^{-2}$) is dominated by the variances of the local vapor change ($0.109\,\mathrm{mm}^2\,\mathrm{h}^{-2}$), vapor convergence ($0.124\,\mathrm{mm}^2\,\mathrm{h}^{-2}$), and the local condensate change ($0.03\,\mathrm{mm}^2\,\mathrm{h}^{-2}$), and the magnitudes of other variances and co-variances are small ($<0.01\,\mathrm{mm}^2\,\mathrm{h}^{-2}$). The linear correlation coefficients between Q_{WVT}, Q_{WVF}, Q_{WVE} and Q_{CM} each individually with P_{s} are 0.54, 0.62, 0.01 and 0.16, respectively. Thus, the variation of surface rain rate can be largely explained by the variances of the local vapor change and vapor convergence. There is no statistically significant correlation between P_{s} and Q_{WVE} because the imposed vapor convergence is responsible

for the variation of P_{s}.

Figure 4 shows the time series of terms related to heating. The time means of S_{RAD}, S_{HT}, S_{HF}, S_{HS} and S_{LH} are -0.036, 0.0002, -0.063, 0.007, and 0.092 $^{\circ}\mathrm{C}\,\mathrm{h}^{-1}$, respectively. In the zonal-mean mass-weighted mean thermal budget, condensational heating (S_{LH}) is nearly balanced by advective cooling (S_{HF}) and radiative cooling (S_{RAD}). The standard deviations of S_{RAD}, S_{HT}, S_{HF}, S_{HS} and S_{LH} are 0.031, 0.08, 0.11, 0.002, and $0.105\,^{\circ}\mathrm{C}\,\mathrm{h}^{-1}$, respectively. The local temperature variations are mainly caused by advective cooling, condensational heating, and radiative cooling. The small standard deviation of S_{HT} denotes little temperature variability in the tropical deep convective regime due to a free tropospheric quasi-equilibrium between convection and large-scale forcing (Zhang, 2003; Donner and Phillips, 2003).

The diurnal composite of P_{s} in the control case in Fig. 5 shows that the largest surface rain rates (>0.4 $\mathrm{mm}\,\mathrm{h}^{-1}$) occur during early morning (hours 0–7), late afternoon, and evening (hours 16–24). The surface rain rate ($\sim0.2\,\mathrm{mm}\,\mathrm{h}^{-1}$) reaches a minimum around hour 13. The comparison of diurnal variations between imposed vertical velocity (Fig. 2) and surface rain rate (Fig. 5) shows that the maximum imposed ascending motion is in phase with the afternoon surface rainfall peak. Since the model in the control case includes the diurnal signals of the large-scale forcing, interactive radiation calculations, and SST, the question is what causes a nocturnal rainfall maximum.

Since the cloud budget contains surface rain rate, the cloud budget is analyzed first. The cloud budget can be expressed by

$$P_{\mathrm{s}} - Q_{\mathrm{CM}} = Q_{\mathrm{WVS}}, \qquad (4)$$
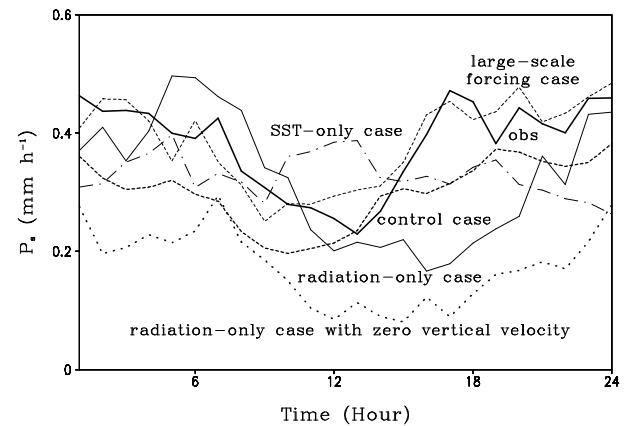

Fig. 5. Diurnal composites of P_{s} in the control case (dark solid), radiation-only case (light solid), large-scale forcing-case (dashed), radiation-only case with zero vertical velocity (dotted), and SST-only case (dot-dashed). Units are $\mathrm{mm}\,\mathrm{h}^{-1}$. Dark dashed line denotes observed P_{s}.
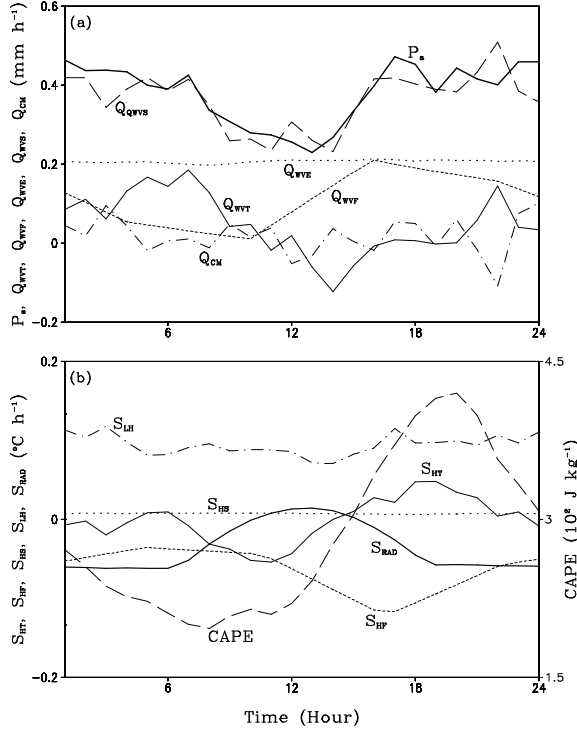
Fig. 6. Diurnal composites of (a) P_s (dark solid), Q_{WVT} (light solid), Q_{WVF} (dashed), Q_{WVE} (dot), Q_{WVS} (long dashed), and Q_{CM} (dashed dot) in water vapor and cloud budgets and (b) S_{HT} (light solid), S_{HF} (dashed), S_{HS} (dot), S_{LH} (dashed dot) and S_{RAD} (dark solid) in heat budget and CAPE (long dashed) simulated in the control case. Units are mm h^{-1} in (a) and °C h^{-1} for heat budget and 10^2 J kg^{-1} for CAPE in (b).

where

$$Q_{WVS} = ([P_{CND}] + [P_{DEP}] + [P_{SDEP}] + [P_{GDEP}]) - ([P_{REVP}] + [P_{MLTS}] + [P_{MLTG}]). \qquad (4a)$$

Here Q_{WVS} is a cloud source or water vapor sink; P_{CND} is the vapor condensation rate; P_{DEP}, P_{SDEP}, and P_{GDEP} are vapor deposition rates for growths of cloud ice, snow, and graupel, respectively; P_{REVP}, P_{MLTS}, and P_{MLTG} are the evaporation rates of rain, melting snow, and liquid from the graupel surface, respectively. In the cloud budget (Fig. 6a), P_s and Q_{WVS} have similar diurnal variations in both phase and magnitude, while Q_{CM} does not have a significant diurnal variation, but instead fluctuates around 0 with amplitudes of 0.1 mm h^{-1} or less. Thus, the diurnal variation of surface rain rate is intimately associated with that of the cloud source. To further examine the diurnal variation of the cloud source, the water vapor budget is next analyzed. The water vapor budget can be written as

$$Q_{WVT} + Q_{WVF} + Q_{WVE} = Q_{WVS}. \qquad (5)$$

In the water vapor budget (Fig. 6a), Q_{WVE} has a constant value of roughly 0.2 mm h^{-1}. Q_{WVF} has its maximum of 0.2 mm h^{-1} at hour 16 when the maximum imposed ascending motion occurs (Fig. 2) and decreases during nighttime, reaching its minimum at hour 10, which is a forced diurnal variation associated with the imposed large-scale vertical velocity. Q_{WVT} attains its maximum of 0.2 mm h^{-1} during hours 5–7 and decreases to its minimum of -0.1 mm h^{-1} at hour 14. Maximum local atmospheric drying ($Q_{WVT} > 0$) occur during hours 5–7 when Q_{WVF} approaches zero. Thus, the peak of Q_{WVS} in early morning is associated with local atmospheric drying, whereas the peak in the late afternoon is caused by the large water vapor convergence associated with the imposed ascending motion.

To analyze the diurnal thermal processes associated with the nocturnal peak of surface rainfall, the diurnal composites of zonal-mean mass-weighted mean thermal budget and zonally-averaged convective available potential energy (CAPE) for reversible moist adiabatic process (Li et al., 2002c) are shown in Fig. 6b. The solar radiative heating reaches its maximum around noon, and it starts to decrease in magnitude in the afternoon. The net radiation becomes cooling around hour 15 when the infrared cooling rate is larger than the solar heating rate. The net radiative cooling reaches its maximum rate after hour 18 after the sunset. The advective cooling (Q_{HF}) associated with the imposed ascending motion in the afternoon also acts to lower local temperature. Similar cooling rates from Q_{HF} and Q_{RAD} occur from hour 18 to hour 8. Thus, the radiative and advective cooling lower local temperature ($Q_{HT} > 0$) from noon to midnight. Significant cooling appears in the mid-troposphere from noon to late afternoon (not shown), which halts the increase of CAPE around hour 20. Continuous radiative and advective cooling causes a significant release of CAPE, a clear signal for destabilizing the atmosphere. The CAPE is transferred to energize nocturnal convective development.

4. Analysis of diurnal variations with sensitivity simulations

To examine the effects of diurnal variations of radiation, vertical velocity, and SST on the formation of the nocturnal rainfall peak, three additional cases (radiation-only, large-scale forcing-only, and SST-only) are conducted and compared with the control case (see Table 1 and section 2 for the designs of these sensitivity experiments). The diurnal composites in Fig. 5 show that the surface rain rates in the large-scale forcing-only case and the control case have similar diurnal evolution in both their phases and am-
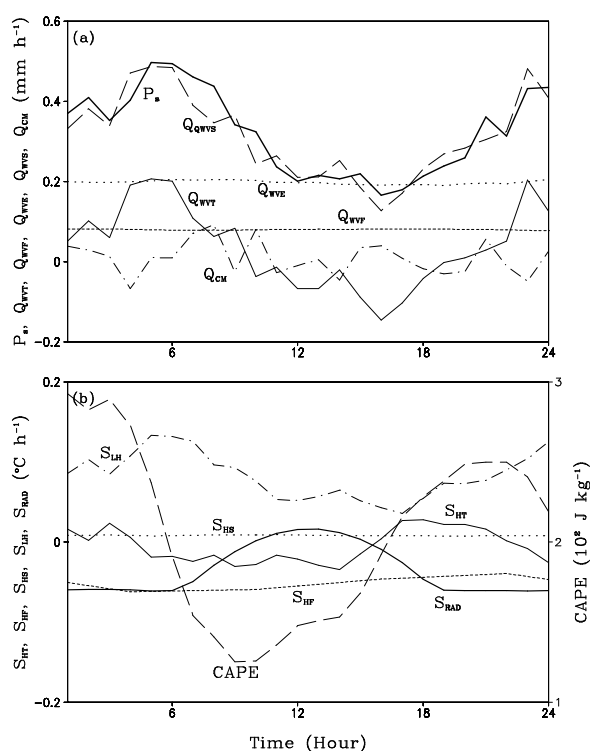
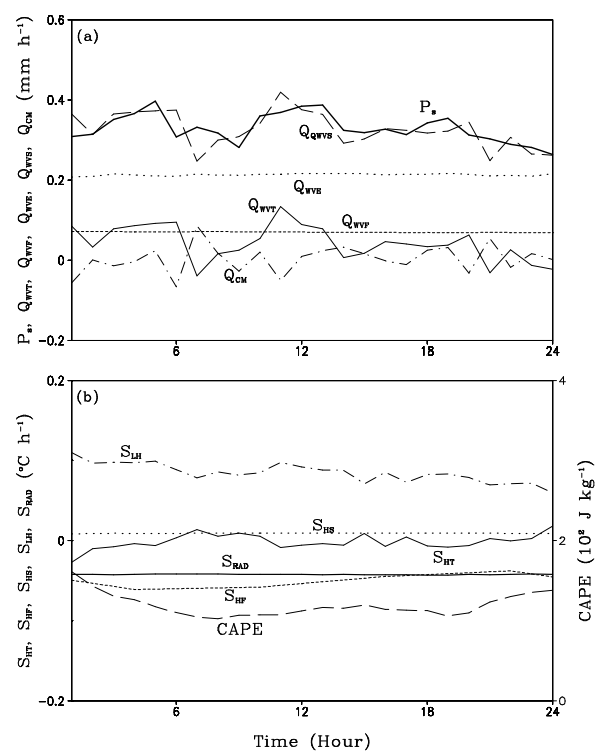**Fig. 7.** As in Fig. 6 except for the radiation-only case.

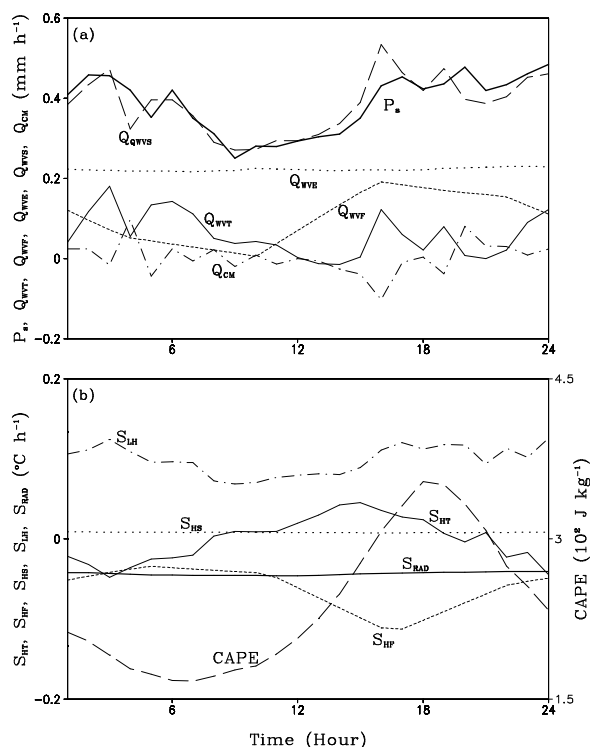**Fig. 9.** As in Fig. 6 except for the SST-only case.

Fig. 8. As in Fig. 6 except for the large-scale forcing only case.

plitudes. The surface rain rate in radiation-only is similar to that in the control case during the first half of the day, whereas it becomes much smaller in afternoon. The surface rain rate in the SST-only case shows relatively large values in morning, at noon, and in late afternoon.

To examine the physical processes that are responsible for the differences and similarities, diurnal composites of cloud, water vapor, heat budget terms, and CAPE in the three sensitivity simulations are calculated and shown in Figs. 7–9. The cloud budgets show that in the three sensitivity simulations, the diurnal variations of surface rain rates are highly correlated with those of vapor condensation and deposition (Q_{WVS}) in both phase and amplitude. The nocturnal peaks of vapor condensation and deposition are associated with those of local atmospheric drying in the water vapor budgets (Figs. 7a, 8a, 9a). The nocturnal enhancement of condensation and deposition is associated with the reduction of saturation mixing ratio by the atmospheric cooling. Thus, the diurnal variations of heat budgets in the three sensitivity experiments will be analyzed next.

In the radiation-only case (Fig. 7b), the latent heat and solar radiative heating overcome the advective cooling due to the imposed time-mean upward motion around noon that results in a local atmospheric warming ($Q_{HT} < 0$). When the solar heating gradu-

ally weakens in the afternoon, the local atmospheric heating rate switches to a cooling. The dominant infrared cooling after sunset maintains the local atmospheric cooling. Thus, the local atmospheric cooling ($Q_{HT} > 0$) lasts from hour 16 to hour 22. The local atmospheric cooling continues in the early morning as the advective cooling and infrared cooling are stronger than the latent heating. The atmospheric cooling causes a significant release of CAPE. In the large-scale forcing-only case (Fig. 8b), the weakening of latent heat causes the local atmospheric cooling in the later morning. The cooling reaches its peak around hour 15 mainly due to intensification of the advective cooling associated with the imposed upward motion. The peak of the atmospheric cooling leads the peak of the advective cooling by 1–2 hours because of the enhancement of the latent heating associated with the peak of the advective cooling. The overall cooling is mainly maintained by the advective cooling. The atmospheric cooling reduces the CAPE as the unstable energy is consumed for convective development. In the SST-only case (Fig. 9b), the local atmospheric cooling and warming rates and the amplitudes of CAPE are much lower than those in the radiation-only case and the large-scale forcing-only case as the latent heat is nearly balanced by the advective and radiative cooling.

The simulations in this study are only for a tropical oceanic deep convective regime. The budget statistics could be different for other synoptic situations. To examine the impact of large-scale forcing on the nocturnal rainfall peak, another radiation-only case (Fig. 10) is tested with imposed zero vertical velocity and horizontal advection, and mean zonal wind (see Table 1 and section 2) and compared with the radiation-only case to study the genesis of the nocturnal rainfall peak. The nocturnal rainfall peak occurs at midnight with a secondary maximum at hour 7 (Fig. 5), which is similar to that in the radiation-only case although the magnitudes of time-mean surface rain rates are different due to different vertical velocities. The similar diurnal variations of surface rainfall, cloud, and water vapor budgets result from the similar diurnal variations of heat budgets between the two experiments, while the atmospheric cooling in the later afternoon is much weaker as a result of the lack of advective cooling associated with the large-scale upward motion. The similarity of diurnal variations in surface rain rates in the two cases shows that the diurnal variation of radiation is an important process in the development of nocturnal rainfall when diurnal variations of large-scale forcing are absent. The difference in time-mean surface rain rates between the two cases suggests that the time-mean large-scale vertical velocity impacts the amplitude of time-mean surface rain rate.
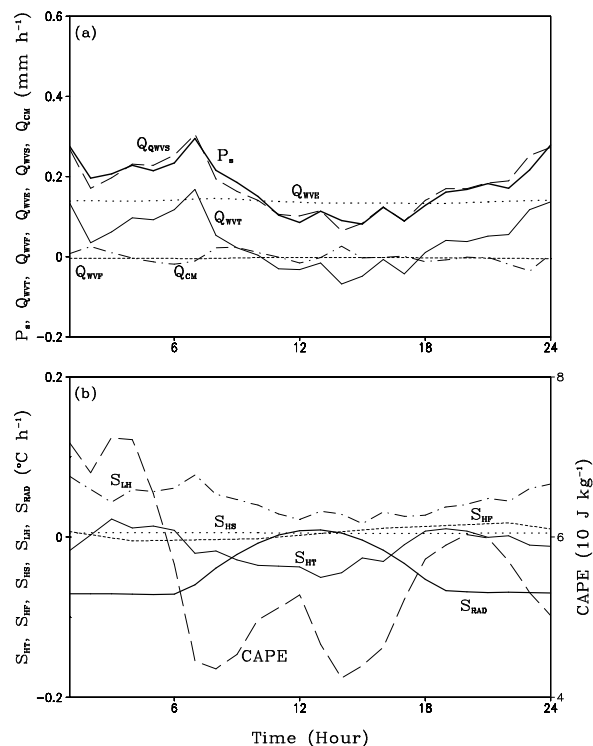

Fig. 10. As in Fig. 6 except for the radiation-only case with zero large-scale vertical velocity. The units of CAPE are 10 J kg^{-1}.

5. Summary

The surface rainfall processes and associated diurnal variations in the tropical convective regime are examined by analyzing hourly zonal-mean data from a series of two-dimensional cloud-resolving model simulations. The water vapor and cloud budgets, thermal budget, and convective available potential energy are examined to quantitatively identify the roles of the diurnal variations of radiation and large-scale circulations on the formation of the nocturnal rainfall peak. In the control experiment, the model is forced by the imposed large-scale vertical velocity, zonal wind, and horizontal advection obtained from TOGA COARE data. The model is integrated for 21 days in the control and sensitivity experiments. A comparison of the observations and control experiment shows that the model simulates thermodynamics and surface rain rate reasonably well. Four sensitivity experiments with diurnally-varying radiation only, diurnally-varying large-scale forcing only, diurnally-varying SST only, and diurnally-varying radiation only using zero large-scale vertical velocity are conducted and compared to the control simulation. The main results include:

(1) The results in the control experiment show that

21-day mean surface rain rate is mainly contributed to by the surface evaporation rate and vapor convergence associated with the imposed large-scale vertical velocity. The 21-day mean thermal budget shows that the condensational heating is nearly balanced by advective and radiative cooling. The variance of the surface rain rate is mainly contributed to by the variances of local vapor change and vapor convergence. Standard deviations of each case reveal that radiative cooling, advective cooling, and condensational heating are important in thermal variability.

(2) Comparison between the sensitivity experiments and the control experiment shows that the experiments with diurnally varying radiation and diurnally varying large-scale forcing produce a nocturnal rainfall peak. Further analysis of heat budgets reveals that the infrared cooling after sunset and advective cooling associated with imposed upward motion are major processes that are responsible for falling air temperatures, which reduces saturation specific humidity and enhances vapor condensation and deposition. The increased vapor condensation leads to the nocturnal peak of surface rainfall.

It should be noted that the high-frequency temporal variability, along with spatial distributions such as individual clouds and associated dynamic and thermodynamic patterns, might be distorted in a 2D model setup. Although Grabowski et al. (1998) compared three-dimensional (3D) and 2D simulations and showed similar evolution in their thermodynamic fields, surface heat fluxes, and precipitation, 3D model simulations may be needed to compare with 2D model simulations to identify dominant processes in diurnal rainfall variations. Another limitation of this study is that the diurnal variation of surface rain rate is only analyzed for a tropical deep convective regime over the open ocean. Therefore, further simulations of diurnal variations with 3D cloud-resolving models should be carried out over different regions to study whether these 2D results for tropical oceanic convection can be applied to 3D simulations over different regions.

REFERENCES

Chou, M.-D., and M. J. Suarez, 1994: An efficient thermal infrared radiation parameterization for use in general circulation model. NASA Tech. Memo. 104606, Vol. 3, 85pp. [Available from NASA/Goddard Space Flight Center, Code 913,Greenbelt, MD 20771.]

Chou, M.-D., D. P. Kratz, and W. Ridgway, 1991: Infrared radiation parameterization in numerical climate models. *J. Climate*, **4**, 424–437.

Chou, M.-D., M. J. Suarez, C.-H. Ho, M. M.-H. Yan, and K.-T. Lee, 1998: Parameterizations for cloud overlapping and shortwave single scattering properties for use in general circulation and cloud ensemble models. *J. Atmos. Sci.*, **55**, 201–214.

Cui, X., and X. Li, 2006: Role of surface evaporation in surface rainfall processes. *J. Geophys. Res.*, **111**, doi:10.1029/2005JD006876.

Dai, A., 2001: Global precipitation and thunderstorm frequencies. Part II: Diurnal variations. *J. Climate*, **14**, 1112–1128.

Donner, L. J., and V. T. Phillips, 2003: Boundary layer control on convective available potential energy: Implications of cumulus parameterization. *J. Geophys. Res.*, **108**(D22), 4701, doi: 10.1029/2003JD003773.

Gao, S., F. Ping, X. Li, and W.-K. Tao, 2004: A convective vorticity vector associated with tropical convection: A 2D cloud-resolving modeling study. *J. Geophys. Res.*, **109**, D14106, doi:10.1029/2004JD004807.

Gao, S., X. Cui, Y. Zhou, and X. Li, 2005: Surface rainfall processes as simulated in a cloud resolving model. *J. Geophys. Res.*, **110**, D10202, doi: 10.1029/2004JD005467.

Gao, S., F. Ping, and X. Li, 2006a: Cloud microphysical processes associated with the diurnal variations of tropical convection: A 2D cloud resolving modeling study. *Meteor. Atmos. Phys.*, **91**, 9–16.

Gao, S., F. Ping, and X. Li, 2006b: Tropical heat/water quasi-equilibrium and cycle as simulated in a 2D cloud resolving model. *Atmos. Res.*, **79**, 15–29.

Grabowski, W. W., X. Wu, and M. W. Moncrieff, 1996: Cloud-resolving model of tropical cloud systems during Phase III of GATE. Part I: Two-dimensional experiments. *J. Atmos. Sci.*, **53**, 3684–3709.

Grabowski, W. W., X. Wu, M. W. Moncrieff, and W. D. Hall, 1998: Cloud-resolving model of tropical cloud systems during Phase III of GATE. Part II: Effects of resolution and the third spatial dimension. *J. Atmos. Sci.*, **55**, 3264–3282.

Gray, W. M., and R. W. Jacobson, 1977: Diurnal variation of deep cumulus convection. *Mon. Wea. Rev.*, **105**, 1171–1188.

Kraus, E. B., 1963: The diurnal precipitation change over the sea. *J. Atmos. Sci.*, **20**, 546–551.

Krueger, S. K., 1997: Intercomparison of multi-day simulations of convection during TOGA COARE with several cloud-resolving models. Preprints, *22nd Conf. on Hurricanes and Tropical Meteorology*, Ft. Collins, Colorado, Amer. Meteor. Soc., 63–64.

Krueger, S. K., Q. Fu, K. N. Liou and H.-N. S. Chin, 1995: Improvement of an ice-phase microphysics parameterization for use in numerical simulations of tropical convection. *J. Appl. Meteor.*, **34**, 281–287.

Li, X., C.-H. Sui, K.-M. Lau, and M.-D. Chou, 1999: Large-scale forcing and cloud-radiation interaction in the tropical deep convective regime. *J. Atmos. Sci.*, **56**, 3028–3042.

Li, X., C.-H. Sui, and K.-M. Lau, 2002a: Precipitation efficiency in the tropical deep convective regime: A 2-D cloud resolving modeling study. *J. Meteor. Soc. Japan*, **80**, 205–212.

Li, X., C.-H. Sui, and K.-M. Lau, 2002b: Dominant cloud microphysical processes in a tropical oceanic convective system: A 2-D cloud resolving modeling study. *Mon. Wea. Rev.*, **130**, 2481–2491.

Li, X., C.-H. Sui, and K.-M. Lau, 2002c: Interactions between tropical convection and its embedding environment: An energetics analysis of a 2-D cloud resolving simulation. *J. Atmos. Sci.*, **59**, 1712–1722.

Lin, Y.-L., R. D. Farley, and H. D. Orville, 1983: Bulk parameterization of the snow field in a cloud model. *J. Climate Appl. Meteor.*, **22**, 1065–1092.

Liu, C., and M. W. Moncrieff, 1998: A numerical study of the diurnal cycle of tropical oceanic convection. *J. Atmos. Sci.*, **55**, 2329–2344.

Moncrieff, M. W., S. K. Krueger, D. Gregory, J.-L. Redelsperger, and W.-K. Tao, 1997: GEWEX Cloud System Study (GCSS) Working Group 4: Precipitating Convective Cloud Systems. *Bull. Amer. Meteor. Soc.*, **78**, 831–845.

Petch, J. C., and M. E. B. Gray, 2001: Sensitivity studies using a cloud-resolving model simulation of the tropical west Pacific. *Quart. J. Roy. Meteor. Soc.*, **127**, 2287–2306.

Randall, D. A., Harshvardhan, and D. A. Dazlich, 1991: Diurnal variability of the hydrologic cycle in a general circulation model. *J. Atmos. Sci.*, **48**, 40–62.

Rutledge, S. A., and P. V. Hobbs, 1983: The mesoscale and microscale structure and organization of clouds and precipitation in midlatitude cyclones. Part VIII: A model for the "seeder-feeder" process in warm-frontalrainbands. *J. Atmos. Sci.*, **40**, 1185–1206.

Rutledge, S. A., and P. V. Hobbs, 1984: The mesoscale and microscale structure and organization of clouds and precipitation in midlatitude cyclones. Part XII: A disgnostic modeling study of precipitation developmentin narrow cold-frontal rainbands. *J. Atmos. Sci.*, **41**, 2949–2972.

Short, D. A., P. A. Kucera, B. S. Ferrier, J. C. Gerlach, S. A. Rutledge, and O. W. Thiele, 1997: Shipboard radar rainfall pattern within the TOGA COARE IFA. *Bull. Amer. Meteor. Soc.*, **78**, 2817–2836.

Soong, S. T., and Y. Ogura, 1980: Response of tradewind cumuli to large-scale processes. *J. Atmos. Sci.*, **37**, 2035–2050.

Soong, S. T., and W. K. Tao, 1980: Response of deep tropical cumulus clouds to mesoscale processes. *J. Atmos. Sci.*, **37**, 2016–2034.

Sui, C.-H., K.-M. Lau, W.-K. Tao, and J. Simpson, 1994: The tropical water and energy cycles in a cumulus ensemble model. Part I: Equilibrium climate. *J. Atmos. Sci.*, **51**, 711–728.

Sui, C.-H., K.-M. Lau, Y. N. Takayabu, and D. Short, 1997: Diurnal variations in tropical oceanic cumulus convection during TOGA COARE. *J. Atmos. Sci.*, **54**, 639–655.

Sui, C.-H., X. Li, and K.-M. Lau, 1998: Radiative-convective processes in simulated diurnal variations of tropical oceanic convection. *J. Atmos. Sci.*, **55**, 2345–2359.

Tao, W.-K., and J. Simpson, 1993: The Goddard cumulus ensemble model. Part I: Model description. *Terr. Atmos. Oceanic Sci.*, **4**, 35–72.

Tao, W.-K, J. Simpson, and M. McCumber, 1989: An ice-water saturation adjustment. *Mon. Wea. Rev.*, **117**, 231–235.

Tao, W.-K., S. Lang, J. Simpson, C.-H. Sui, B. Ferrier, and M.-D. Chou, 1996: Mechanisms of cloud-radiation interaction in the tropics and midlatitude. *J. Atmos. Sci.*, **53**, 2624–2651.

Weller, R. A., and S. P. Anderson, 1996: Surface meteorology and air-sea fluxes in the western equatorial Pacific warm pool during TOGA COARE. *J. Climate*, **9**, 1959–1990.

Wu, X., W. W. Grabowski, and M. W. Moncrieff, 1998: Long-term evolution of cloud systems in TOGA COARE and their interactions with radiative and surface processes. Part I: Two-dimensional cloud-resolving model. *J. Atmos. Sci.*, **55**, 2693–2714.

Xu, K.-M., and D. A. Randall, 1995: Impact of interactive radiative transfer on the macroscopic behavior of cumulus ensembles. Part II: Mechanisms for cloud-radiation interactions. *J. Atmos. Sci.*, **52**, 800–817.

Xu, K.-M., and D. A. Randall, 1996: Explicit simulation of cumulus ensembles with the GATE Phase III data: Comparison with observations. *J. Atmos. Sci.*, **53**, 3710–3736.

Zhang, G. J., 2003: Convective quasi-equilibrium in the tropical western Pacific: Comparison with midlatitude continental environment. *J. Geophys. Res.*, **108**(D19), 4592, doi: 10.1029/2003JD003520.

Zhang, M. H., and J. L. Lin, 1997: Constrained variational analysis of sounding data based on column-integrated budgets of mass, heat, moisture, and momentum: Approach and application to ARM measurements. *J. Atmos. Sci.*, **54**, 1503–1524.